Available online at www.sciencedirect.com
SCIENCE DIRECT®
ELSEVIER
International Journal of Rock Mechanics & Mining Sciences 42 (2005) 924–932
International Journal of Rock Mechanics and Mining Sciences
www.elsevier.com/locate/ijrmms

Poroelastic behaviour of physical properties in Rotliegend sandstones under uniaxial strain

U. Trautwein*, E. Huenges

GeoForschungsZentrum, Potsdam, Germany

Accepted 3 May 2005
Available online 15 July 2005

Abstract

Laboratory experiments simulating reservoir depletion and reinjection of fluids have been conducted on Rotliegend reservoir sandstones. Pore pressure dependence of petrophysical properties have been measured under uniaxial strain boundary conditions, i.e., zero lateral strain at constant overburden pressure. Permeability, formation resistivity factor, and compressional as well as shear wave velocities were recorded simultaneously and continuously during deformation in direction of maximum principal stress. The results show that the stress development is specific for different sandstones depending on the efficiency of pore pressure. The stress anisotropy increases with decreasing pore pressure, leading to stress-induced anisotropy of pore structure with preferred closure of horizontally oriented pore space. Permeability decline of initially lower permeability sandstones indicate the opening of axially oriented pores at lower pore pressure.

1. Introduction

Permeability is a key parameter describing the quality of geothermal reservoirs. It depends strongly on pore structure, which is assumed to change with effective stress. Therefore, understanding the pore pressure-induced alteration of rock structure and permeability is crucial for reservoir exploration and exploitation.

The concurrent measurement of additional petrophysical properties, e.g., electrical or mechanical properties, parallel with permeability measurement during deformation, provides important information for the understanding of permeability development from the microstructural point of view. It also helps to find correlations as well as discrepancies between these properties. Reliable correlations are required for log interpretation as well as for 4D monitoring of hydrocarbon and geothermal reservoirs.

Development of permeability depends on the stress path applied to the rock, defined as the change in effective horizontal stress to change in effective overburden stress (see [1–4]). The importance of stress anisotropy especially for permeability but also for other structure-sensitive parameters is well documented in the literature (e.g. [5,6]). Heiland [7] recently compiled the extensive amount of experimental work done on stress-dependent permeability for hydromechanical coupling.

Uniaxial strain boundary conditions are usually assumed for reservoir compaction (e.g. [1,8]), i.e., no lateral strain occurs due to crustal confinement, and overburden stress does not change during production of the reservoir. Therefore, changes of reservoir fluid pressure will lead to changes in effective stress and consequently to reservoir compaction and alteration of petrophysical properties.

In laboratory experiments, we varied the pore pressure under uniaxial strain boundary conditions to simulate reservoir depletion and reinjection of fluids. Stress, strain, permeability, formation resistivity factor and compressional as well as shear wave velocities are

*Corresponding author. Geological Institute RWTH Wüllnerstraße 2, D-52062 Aachen, Germany. Tel.: +49 241 80 95732.
E-mail address: trautwein@geol.rwth-aachen.de (U. Trautwein).

1365-1609/$ - see front matter © 2005 Elsevier Ltd. All rights reserved.
doi:10.1016/j.ijrmms.2005.05.016

measured continuously and simultaneously throughout the experiments.

The experiments were performed on sandstone core samples from the Rotliegend formation of the Northeast German Basin. The cores are from 4180 to 4200 m depth of the Groß Schönebeck well drilled in 1990 for gas exploration. The well is located 50 km NE of Berlin. It was reopend in 2000 to study the feasibility of geothermal energy use in sedimentary basins [9].

2. Sample material

Three core samples (GS10, GS19 and GS20) were selected covering a representative range of porosities and permeabilities of deep Rotliegend sandstones. At unloaded condition, porosities and permeabilities range from 18.3% to 9.8% and from more than 100 to 3 mD, respectively. Macroscopically bedding from millimetre- to centimetre-scale with dip angles between 0° and 30° is observed. Grain size and sorting vary within sedimentary bedding from well sorted fine-grained to medium sorted fine- to medium-grained layers. The detrital components are mainly well rounded to subrounded. The dominant detrital fraction is monocrystalline quartz with 10–20 vol% feldspar grains and 10–20 vol% rock fragments. Various cement generations are observed (quartz, feldspar, illite, carbonate, anhydrite) resulting in a reduction of free pore space (Fig. 1). Small contents of illite occurred in all samples with platy and fibrous morphology, and could affect the petrophysical properties, especially the permeability.

Pore structure was investigated by pore size distributions obtained by image analysis of thin-sections as well as by mercury intrusion. While mercury intrusion records the narrow throats of pore space that control the transport of fluid, pore space observed in thin-sections belongs to pore bodies, which correlate with bulk porosity. Pore radii from thin-sections are calculated as pore area equivalent circle radii. Fig. 2 shows the relative radii distributions of pore throats and bodies of the three sandstones. The relative pore radii maxima from thin-section are located between 20 and 40 μm for all sandstones, even though porosity is different. With declining porosity and permeability the maximum of pore radii distribution from mercury intrusion is shifted to smaller radii and the deviation between the maxima of pore bodies and pore throats increases. This deviation indicates that porosity is existent but poorly connected.

For our experiments we prepared cylindrical samples with a length to diameter ratio equal to 2:1. The experimental set-up (see below) requires sample diameter of 50 mm. For this reason, the specimens had to be prepared with the cylinder axis parallel to the core axis. Consequently, the sedimentary bedding of the sandstones is oriented normal to the cylinder axis. The direction of measurement of permeability, formation resistivity factor and ultrasonic wave velocities is normal to bedding in the direction of maximum principal stress.

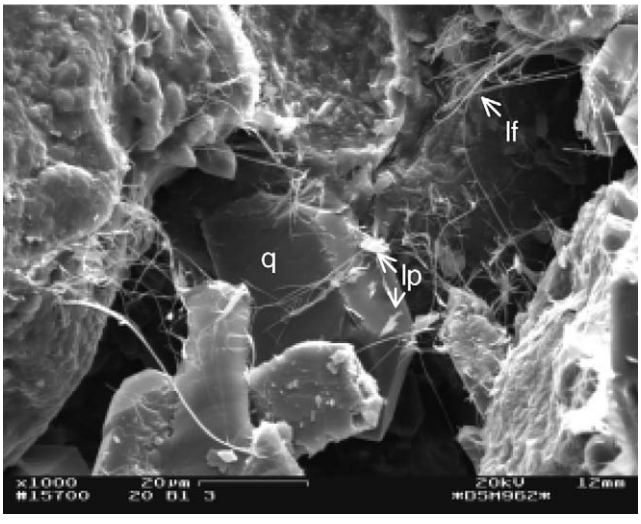

Fig. 1. SEM-image of authigenic quartz (q) and two generations of illite, platy (Ip) and fibrous (If), reduce the free pore space between detritical quartz grains.

3. Test equipment and experimental design

The experiments were performed in a triaxial press for rock mechanics (MTS) equipped with constructions for simultaneous and continuous measurement of porosity, permeability and electrical resistivity during the deformation of the rock sample. The velocity of ultrasonic waves is measured at specific points during the experiment.

Uniform confining pressure P_c acts from all sites on the surface of the specimen. A heat-shrink tube separates the confining hydraulic oil from the pore fluid system. The axial piston applies an additional differential stress σ_{dif} to the coplanar sample ends. The axial actuator as well as the confining pressure actuator are servo-controlled and can be moved in stress as well as in strain control mode.

The following external stresses were applied to the samples:

$$P_c = \sigma_2 = \sigma_3, \quad (1)$$

$$\sigma_1 = P_c + \sigma_{dif}. \quad (2)$$

The maximum principal stress σ_1 is oriented in axial direction. Intermediate and minor stresses (σ_2 und σ_3) are of equal size and correspond to the confining pressure P_c. In this paper, the effective stress σ_{eff} is defined as the difference between external stress and

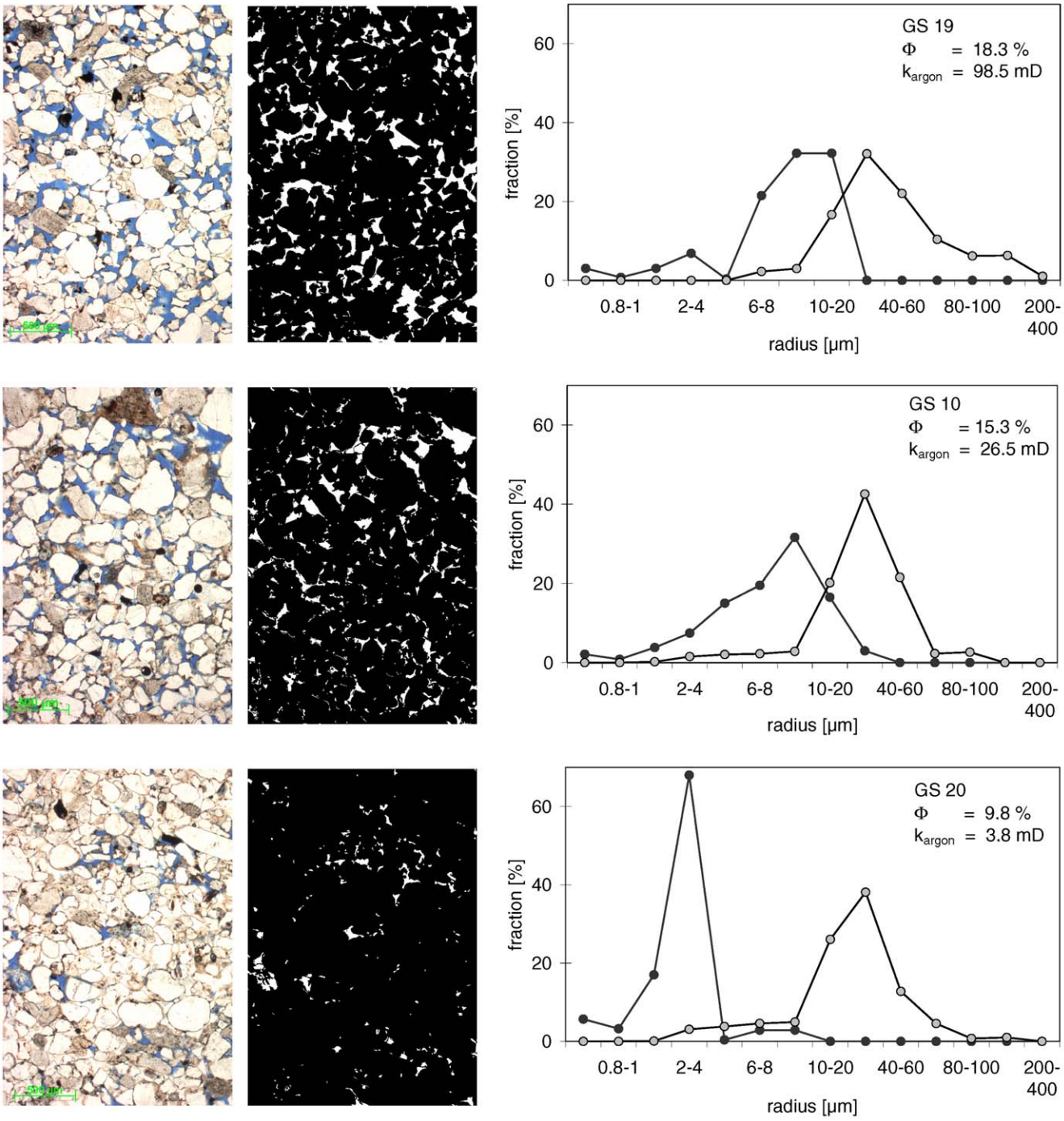

Fig. 2. Thin-sections and pore radii distribution measured by image analysis (grey line) and mercury intrusion (black line) for the three sandstone samples with values of porosity (Φ in %) and permeability (k in mD). Images of thin-sections are shown in transmitted light (left) and as binary image (middle) with pore space plotted in white colour.

internal pore pressure P_p multiplied by the effective stress coefficient α for stress–strain relation:

$$\sigma_{eff} = \sigma - \alpha P_p. \tag{3}$$

Because α was not measured directly it was calculated from the pore pressure-induced development of external stresses using an uniaxial strain version of Hooke's law for poroelasticity [10]:

$$\sigma_2 = \sigma_3 = \frac{\upsilon}{1-\upsilon}(\sigma_1 - \alpha P_P) + \alpha P_P, \tag{4}$$

$$\alpha = \frac{\Delta P_c}{\Delta P_P} - \frac{\upsilon}{1-2\upsilon}\frac{\Delta \sigma_{dif}}{\Delta P_P}. \tag{5}$$

Axial deformation is measured by two extensometers placed on opposite sides covering the centre of the sample. The axial extensometers consist of pins with an initial distance of 50 mm in axial direction. Axial deformation changes the distance between these two pins. Radial strain is determined by measuring circumferential strain with a chain extensometer located around the middle of the cylindrical sample. Porosity is derived from strain measurements assuming that volumetric deformation results entirely from changes in the pore volume, whereas the volume of the matrix material remains constant, i.e., the compressibility of the grains is negligible.

The fluid pump system for internal pore pressure consists of four pump cylinders driven by stepper motors. By using the cylinders in paired control mode it is possible to pump water continuously at controlled pore pressure in axial direction through the rock sample. 0.1 molar NaCl solution is taken as the pore fluid. Using a constant pressure gradient while the inflowing and outflowing fluid volume per time is recorded, permeability can be calculated assuming steady-state conditions. Temperature-dependent fluid viscosity is taken into account.

The main complication of measuring stress-dependent water permeability is the permanent decrease of flow rate even if stress and temperature are constant for long times and no macroscopic deformation occurs. The degree of decline changes non-systematically with stress and flow direction. It is most likely caused by fines mobilisation and pore plugging. To separate this effect from stress-induced changes of permeability, permeability values are corrected for the decrease of permeability observed at constant pore pressure.

The mechanical and fluid pressure systems are fully computer-controlled. Data are collected at constant time intervals as well as event triggered with a set of data taken every minute, every 1 MPa change of confining pressure and every 5 kN change of axial load.

For the measurement of formation resistivity factor alternating current (1 V, 1 kHz) is applied to the fluid saturated sample and the voltage drop is measured in a four-point arrangement. Ohm's law and sample geometry provide the specific sample resistivity, and formation resistivity factor is calculated using Archie's first equation. All resistivity data are corrected to a reference temperature of 25 °C.

Piezoelectric compressional and shear wave transducers (500 kHz) are embedded within the two end caps of the sample holder. The elastic wave velocities are measured by the pulse-transmission technique with wave propagation in axial direction. By using piezoelectric transducers the electrical measurements are disturbed. Consequently, the detection of wave velocities is restricted to selected states of stress with interruption of the electrical measurement for that time. The accuracy of the measurement of elastic wave velocities is 1%.

Table 1
In situ stress condition observed in the Groß Schönebeck well at 4200 m depth

Parameter	Value (MPa)
Axial stress σ_1	100
Minimum horizontal stress σ_3	53
Fluid pressure P_p	45

Table 2
Petrophysical properties of the specimens submitted to in situ stress: $\sigma_1 = 100$ MPa, $P_c = 53$ MPa and $P_p = 45$ MPa

Sample	Φ (%)	K (10^{-15} m^2)	F	v_p (ms^{-1})	v_s (ms^{-1})
GS10	14.9	2.15	22.1	4321	2554
GS19	17.7	16.5	16.8	4090	2372
GS20	9.5	0.14	53.6	4753	2800

After installation of the oven-dry samples (vacuum drying oven, 60 °C, for more than 3 days) in the triaxial press, the pore space and pore pressure system were evacuated and subsequently saturated with 0.1 molar NaCl solution for more than 12 h. The saturation time depends on pore structure. Constant resistivity was taken as criterion for complete saturation.

The specimens were loaded up to an initial state of stress according to the in situ stress condition observed in the Groß Schönebeck well at 4200 m depth (Table 1). Confining pressure corresponds to the minimum horizontal stress, total axial load to the overburden stress, and the internal pore pressure is in accordance with the reservoir fluid pressure. All pressures were increased simultaneously to avoid irreversible sample compaction. The petrophysical properties of the samples at in situ stress level are listed in Table 2. An example of the progression of stress with time during the uniaxial strain experiments is shown in Fig. 3 for sample GS10. Starting from the initial stress state the pore pressure is reduced at 0.05 MPa/min down to 5 MPa, enforcing uniaxial strain boundary conditions. To avoid lateral deformation the confining pressure actuator is moved in lateral strain control. If axial stress is held constant, the differential stress increases as the confining pressure decreases. After ramping up the pore pressure back to the initial value, the load cycle is repeated, because deformation resulting from the first load cycle was found to be always stronger than deformation from the subsequent loads.

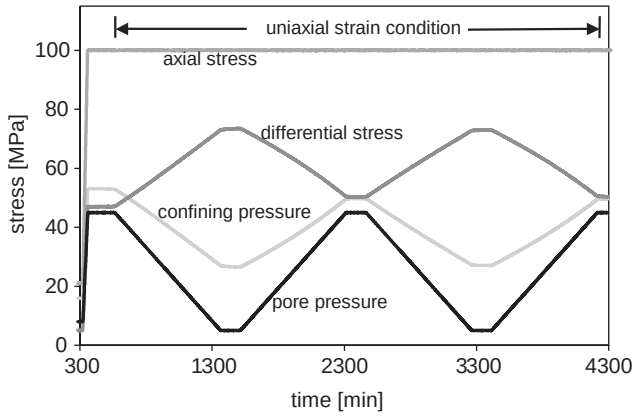

Fig. 3. Development of external stress during pore pressure variation enforcing uniaxial strain boundary conditions for GS10.

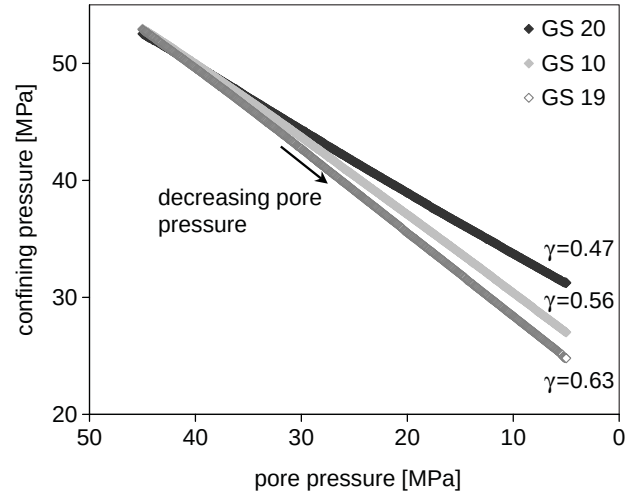

Fig. 4. Decreasing confining pressure for pore pressure reduction under uniaxial strain boundary conditions. The ratio γ is defined as change of confining pressure to change of pore pressure (2nd load).

4. Pore pressure-induced change of effective stress

Under uniaxial strain boundary conditions a decrease in pore pressure changes the effective stress. Due to zero lateral strain the confining pressure decreases with pore pressure. Fig. 4 shows the correlation of confining pressure and pore pressure for the three sandstone samples. Transmitted to the reservoir, the ratio γ between the change of minimum horizontal stress and the change of pore pressure is called the horizontal stress path [8]. The experiments show a stress ratio γ between 0.47 (GS20) and 0.63 (GS19).

The pore pressure-induced change of confining pressure necessary for inhibition of lateral deformation is strongest for the most porous/permeable sample GS19. This reflects the higher efficiency of pore pressure counteracting the external load in high-porosity rocks

Table 3
Calculated effective stress coefficient for pore pressure decrease under uniaxial strain boundary conditions assuming linear poroelasticity

Sample	v_{dyn}	α
GS10	0.22	0.78
GS19	0.24	0.90
GS20	0.21	0.61

and argues for the importance of the effective stress coefficient α for the stress–strain relation. Because the effective stress coefficient α was not measured directly, it was calculated from the pore pressure-induced development of external stresses and the dynamic Poisson's ration v assuming linear poroelasticity (Eq. (5)). The parameter α ranges between 0.61 (GS20) and 0.90 (GS19) (Table 3). The efficiency of pore pressure depends on rock structure and decreases with decreasing porosity and increasing cementation of the sandstone [10].

The differential stress increases by the same amount as the confining pressure decreases in order to hold the total axial load. Fig. 5 shows the effective stress development during the second pore pressure decrease enforcing uniaxial strain boundary conditions. The effective stresses are increasing with decreasing pore pressure. Due to the different efficiency of pore pressure, low-porous sandstones suffer higher mean effective stress while the differential stress is higher for higher porous sandstones. As effective axial stress increases 3.3–4.2 times the effective horizontal stress, the anisotropy of stress state increases with decreasing pore pressure.

5. Macroscopic deformation and porosity

Due to the uniaxial strain boundary conditions the sample only deforms in axial direction. Pore pressure decrease leads to axial compaction of the sandstone sample. Fig. 6 shows the axial strain induced by pore pressure change from in situ condition for the three sandstone samples for the second load cycle. The stress–strain correlation is almost linear with a hysteresis between loading and unloading. The hysteresis is attributed to time-dependent behaviour partly caused by delayed pore pressure equalisation inside the pore space. Such an effect is also observed in ongoing deformation during holding stage at low pore pressure. This behaviour indicates that the pore pressure ramps of 0.05 MPa/min have been too fast for complete pressure equalisation.

Axial deformation for a pore pressure reduction of 40 MPa amount to 0.59 to 1.01 mm/m. Compaction

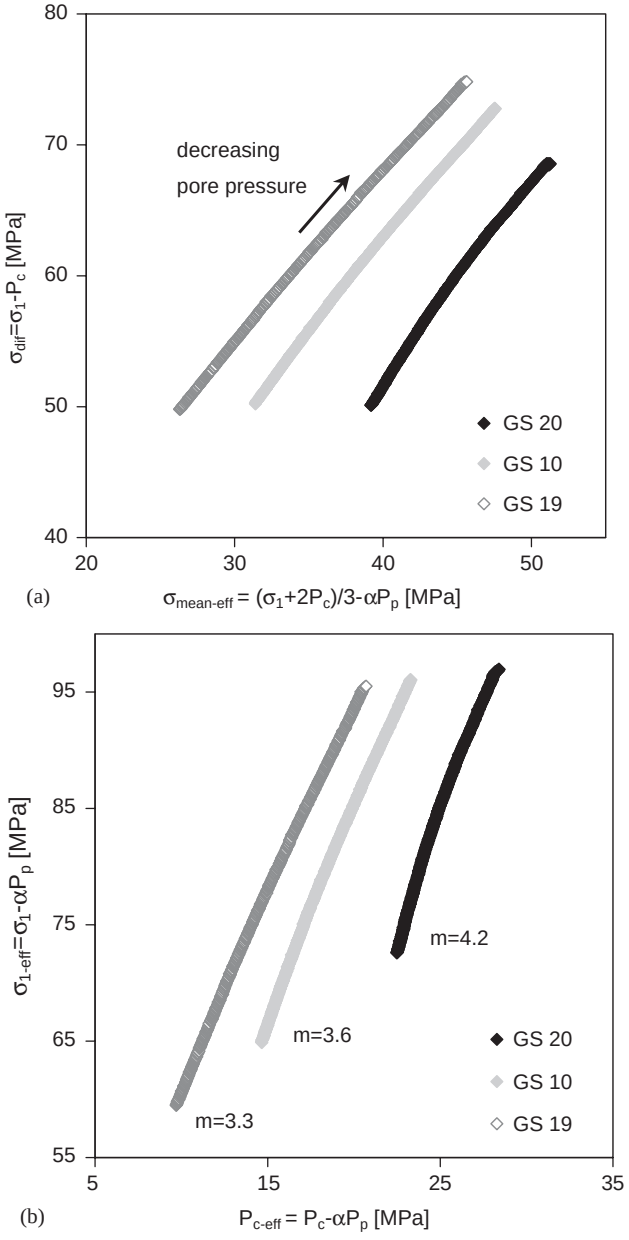

Fig. 5. Development of effective stresses during pore pressure reduction enforcing uniaxial strain boundary conditions (2nd load): (a) differential stress σ_{dif} vs. mean effective stress $\sigma_{mean-eff}$, (b) effective axial stress σ_{1-eff} vs. effective confining pressure P_{c-eff}. The slope m is defined as ratio between the change in effective axial stress to change in effective confining pressure ($m = \Delta\sigma_1/\Delta P_c$).

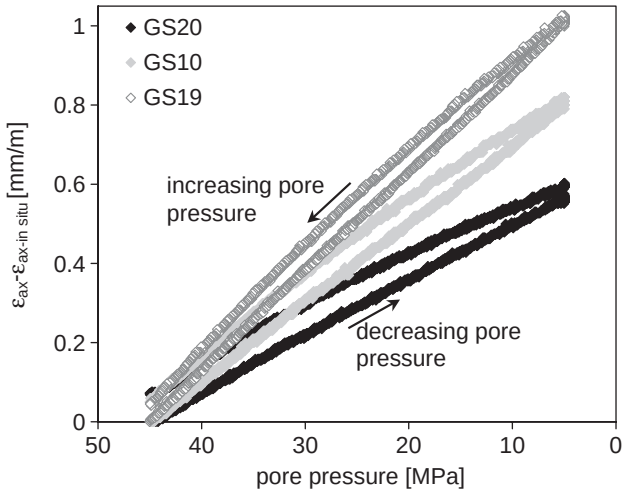

Fig. 6. Axial strain induced by pore pressure variation from in situ condition (2nd load cycle).

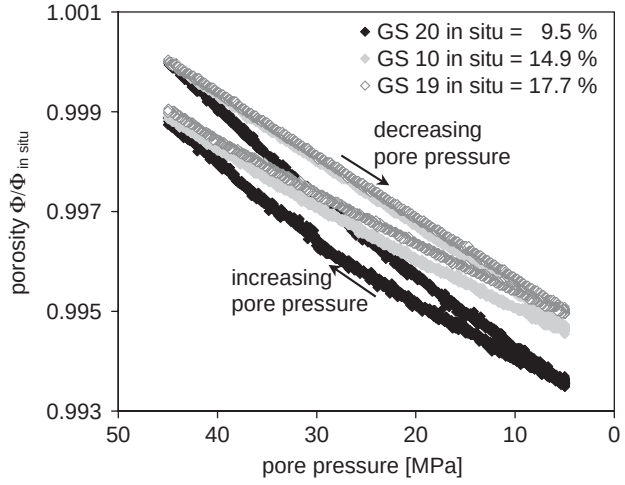

Fig. 7. Relative porosity for pore pressure change enforcing uniaxial strain condition (2nd load). Porosity is based on the in situ values.

clearly correlates with initial porosity: axial strain of the rock with initially high porosity (GS19) is nearly twice the axial strain of the sandstone with half the initial porosity (GS20).

Pore pressure-dependent porosity is plotted in Fig. 7. To allow the comparison of different sandstones the measured porosity is normalised by dividing it by the initial values measured under simulated in situ reservoir stress before pore pressure reduction. These relative changes in porosity are very small. A maximal reduction of 6% was observed. The relative reduction of porosity is stronger for low-porosity sandstones.

6. Microscopic deformation and permeability development

Fig. 8 shows the relative permeability change based on in situ values versus pore pressure. The permeability decrease of about 10% for all samples is very small. The sandstones show different behaviour of permeability at decreasing pore pressure, depending on the initial permeability. While normalised permeability of the most permeable sandstone GS19 decreases linearly with pore pressure and drops to 87% of its in situ value, changes

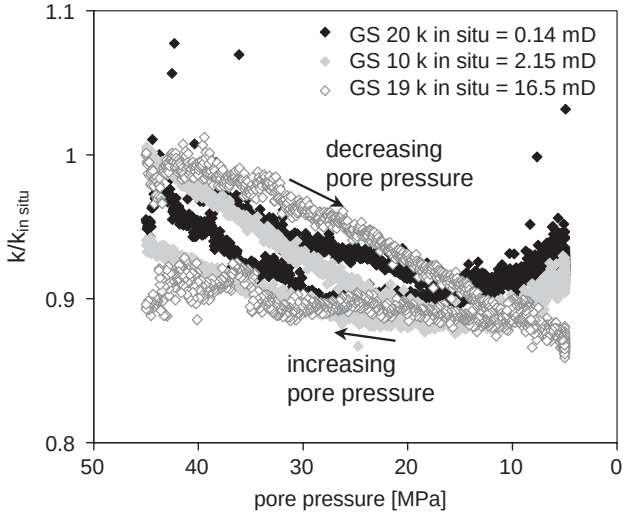

Fig. 8. Permeability change induced by pore pressure change enforcing uniaxial strain condition (1st load). Permeability is normalised by the in situ values. The detectable accuracy of permeability is ±1%.

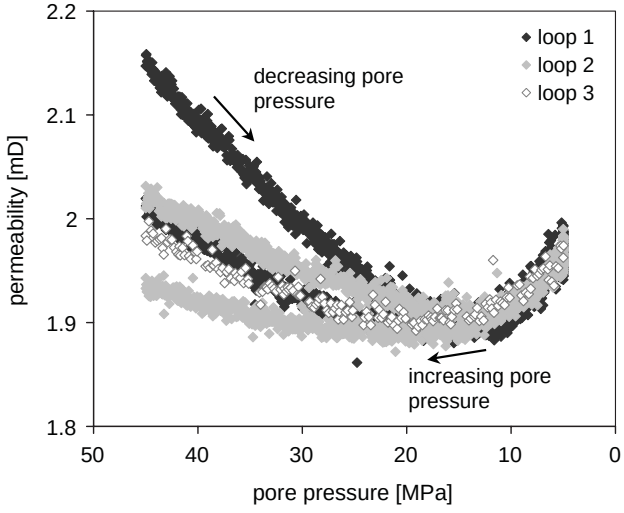

Fig. 9. Non-linear correlation between permeability and pore pressure of Rotliegend sandstone GS10. The increase of permeability at low pore pressure is reversible by increasing pore pressure and repeatable by subsequent loading ramps.

of permeability of the initially lower permeable sandstones GS10 and GS20 are clearly non-linear: permeability decline is stronger at high pore pressure, gets smaller with decreasing pore pressure, and reverses to incline at low pore pressure. The permeability of GS20 gets to a minimum between 17 and 11 MPa with 0.91% of its in situ value and increases afterwards to 0.93% at 5 MPa pore fluid pressure. Permeability of GS10 decreases to 88% of the in situ value at a pore pressure between 15 and 11 MPa followed by an incline to 91% at minimum pore pressure. The permeability incline occurs only for lower permeable sandstones at high stress anisotropy. It is mostly reversible with increasing pore pressure and repeatable for subsequent loading cycles (see also Fig. 9).

The pore pressure-induced permeability does not correlate with deformation and porosity. In the first place, the porosity reduction is too small to account for the total permeability reduction. Moreover, at low pore pressures we observed an increase of permeability with decreasing porosity. Enhanced permeability at high differential stress for low-porosity rocks is well documented in the literature (e.g. [1,12]) but is usually accompanied by macroscopic (measurable) dilation seen in increasing volume before failure. The observed increase in permeability at constant axial compaction with impeded lateral deformation is rather unexpected. Obviously, any explanation for these observations has to include microstructural aspects.

Permeability decline at high pore pressure is attributed to increasing effective axial and effective horizontal stress. Fluid pathways are closed in axial as well as in horizontal direction. Flow channels get more constricted and hydraulic tortuosity increases. Increasing anisotropy of stress leads to increasing orientation of pore space with preferred closure of horizontal orientated pore space. The ratio of effective axial stress and effective horizontal stress is high at low pore pressure and allows the reopening of axially orientated pores.

The process of opening and closing flow channels at decreasing and increasing pore pressure is repeatable (Fig. 9). Since it shows elastic behaviour we assume that it is restricted to grain boundaries. The formation of new cracks is negligible. In fact, no additional cracks have been observed in thin-sections prepared of deformed samples after the experiments.

The results suggest that increasing permeability is restricted to lower permeable sandstones. Due to the larger difference between pore bodies and pore throats (Fig. 2) the opening of pore throats in flow direction can result in remarkable enhancement of hydraulic conductivity. In sandstones with well-connected pore space and high porosity the reduction of permeability prevails due to the ongoing reduction of bulk porosity and horizontal connectivity. Boutéca et al. [11] explain the different permeability behaviour of low and high-porosity rocks as follows: while in low connectivity (low porosity) sandstones any microcrack will contribute to the enhancement of pore connectivity, microfissures will not change the overall connectivity in high connectivity (high porosity) sandstones. Moreover the microcracks will allow grain movements, which in turn will increase the flow path length—tortuosity—and/or reduce the pore throat size [11].

Rhett and Teufel [3] documented experimental results of the effect of reservoir stress path on the compressibility and permeability of two sandstones with initial

porosity range of 13–24%. They observed increasing matrix permeability at stress paths smaller than 0.75–0.50. They emphasised that radial strains remained very small, so that dilation was negligible, and suggested matrix permeability to be related to increasing shear stress with decreasing value for stress path.

The results of our work show clearly that increasing hydraulic connectivity is possible without macroscopic dilation. It already takes place in the elastic regime as the opening and closure of grain boundary-related microcracks is mostly reversible and repeatable. High-stress anisotropy leads to the opening of microcracks in direction of flow, which corresponds to the direction of maximum principal stress.

7. Signature of microstructural deformation from formation resistivity factor and ultrasonic wave velocities

The formation resistivity factor increases almost linearly with decreasing pore pressure (Fig. 10). The relative increase in samples GS10 and GS20 is more than twice the relative increase in GS19. While loading and unloading curves of GS19 are almost identical, GS10 and GS20 show a remarkable hysteresis. Their unloading paths have different slopes: after the first load cycle the formation factor of GS10 is increased by 10%, whereas the formation factor of GS20 is reduced by 5% compared to the in situ values. There seems to be no microstructural effect since small changes in fluid conductivity, which was insufficiently measured for GS10 and GS20, cause considerable changes in formation resistivity factor.

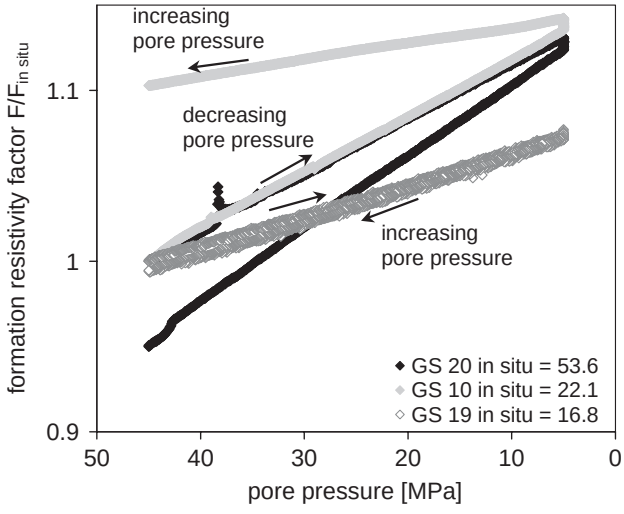

Fig. 10. Relative change of formation resistivity factor F with pore pressure under uniaxial strain boundary conditions (1st load). F is based on the in situ values.

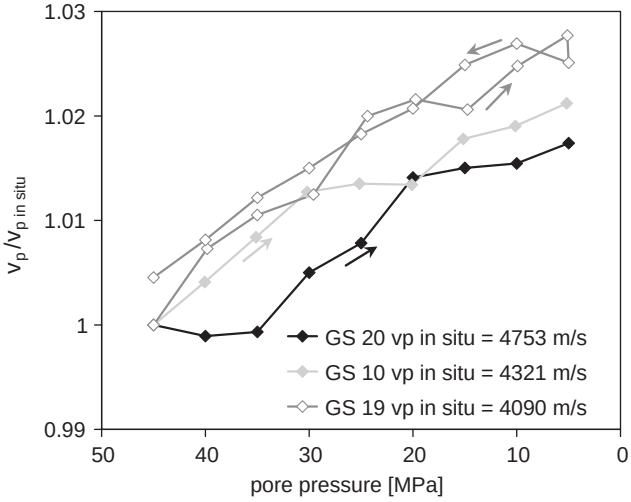

Fig. 11. Relative change of compressional wave velocity with pore pressure decrease enforcing uniaxial strain boundary conditions (3rd load).

The continuous increase of the electrical resistivity does not correlate with the hydraulic conductivity at low pore pressure. This proves that the transport pathways of fluid and electrical current are not the same. The viscous flow of fluid depends on the pore channel size and cross-sectional shape while electrical flow, being purely diffusive, depends mostly on the total cross-sectional area available to conduct the current [13]. Consequently, the fluid flow follows only the larger channels, while electrical current uses all channels [14]. The enhancement of hydraulic conductivity due to the opening of axially oriented pore space does not necessarily result in an increase of electrical conductivity, if the channel was already electrically conductive before or if it has no special contribution to the overall electrical network. If the opening of pore space is only attributed to narrow pores along grain boundaries and no additional cracks are generated, it can be assumed that these pores had never been closed completely for transport of charge. Consequently, electrical resistivity still increases even at low pore pressure in agreement with the ongoing reduction of bulk porosity.

The velocity of ultrasonic waves increases with decreasing pore pressure. Following a pore pressure reduction of 40 MPa, the compressional wave velocity (Fig. 11) increases by 2–3% compared to the in situ value. The shear wave velocity (Fig. 12) increases by 4–6% of in situ value.

Direction of wave propagation corresponds to the direction of maximum principal stress. Due to pore pressure-induced increase of differential stress, axial compaction leads mainly to the closure of horizontal pore space and to the increase of grain contacts perpendicular to axial direction, causing the observed

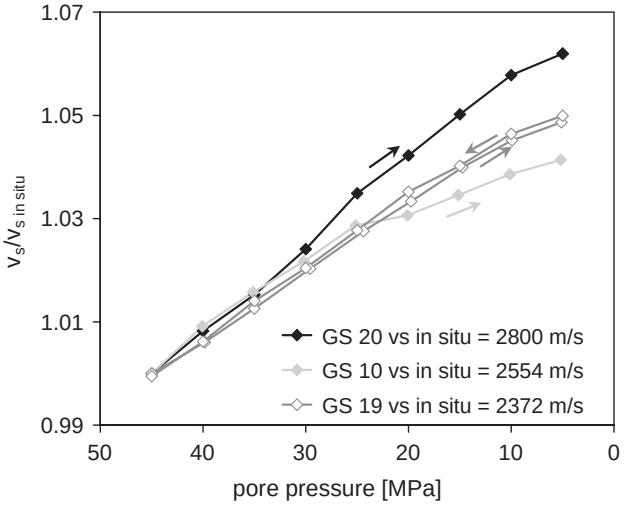

Fig. 12. Relative change of shear wave velocity with pore pressure decrease enforcing uniaxial strain boundary conditions (3rd load).

increase of velocity for compressional and shear waves. The opening of axially oriented grain contacts due to high stress anisotropy is not detectable by the axially propagating waves.

8. Conclusions

Change of pore pressure under uniaxial strain boundary conditions induces a change of effective stress. This results in deformation and is visible in all macroscopic properties: porosity, permeability, formation resistivity factor, compressional and shear wave velocities.

With decreasing pore pressure the increase of effective axial stress is stronger than the increase of effective horizontal stress, resulting in increasing anisotropy of the stress state. This anisotropic stress condition leads to preferred closure of horizontally orientated pore space and opening of vertically orientated pore space along grain contacts at low pore pressure. The anisotropy of microstructure increases with decreasing pore pressure.

Due to the experimental set-up, the anisotropy of microstructure could not be measured directly since all parameters were determined only in axial direction corresponding to the direction of maximum principal stress. The only evidence for opening of axial oriented pores is the enhanced hydraulic conductivity for less permeable sandstones at low pore pressure.

The formation resistivity factor shows a constant increase with decreasing pore pressure. No enhancement of electrical conductivity is observed at low pore pressure. This shows the stronger dependence of hydraulic conductivity on effective pore radii compared to electrical conductivity, which still decreases even at low pore pressure parallel with the ongoing reduction of bulk porosity.

As the direction of open pore space is parallel to the direction of ultrasonic wave propagation the increasing microstructural anisotropy is not detectable in compressional and shear wave velocity measurements.

To allow a better analysis of microstructural deformation and permeability development under anisotropic stress conditions, future experiments should include measurements of petrophysical properties in direction of minimum principal stress as well.

References

[1] Khan M, Teufel LW. The effect of geological and geomechanical parameters on reservoir stress path and its importance in studying permeability anisotropy. SPE Reserv Eval Eng 2000;3(5):394–400.
[2] Ruistuen H, Teufel LW, Rhett D. Influence of reservoir stress path on deformation and permeability of weakly cemented sandstone reservoirs. SPE Reserv Eval Eng 1999;2(3):266–72.
[3] Rhett DW, Teufel LW. Effect of reservoir stress path on compressibility and permeability of sandstones. Society of the Petroleum Engineers paper 24756, 1992.
[4] Schutjens PMTM, de Ruig H. The influence of stress path on compressibility and permeability of an overpressurized reservoir sandstone: some experimental data. Phys Chem Earth 1997; 22(1–2):97–103.
[5] Al-Harthy SS, Jing XD, Marsden JR Dennis JW. Petrophysical properties of sandstone under true-triaxial stress I: directional transport characteristics and pore volume change. Society of the Petroleum Engineers paper 57287, 1999.
[6] Morita N, Gray KE, Sroujl FAA, Jogi PN. Rock-property changes during reservoir compaction. Society of the Petroleum Engineers paper 13099, 1992.
[7] Heiland J. Laboratory testing of coupled hydro-mechanical processes during rock deformation. Hydrogeol J 2003;11:122–41.
[8] Hettema MHH, Schutjens PMTM, Verboom BJM, Gussinklo HJ. Production-induced compaction of a sandstone reservoir: the strong influence of stress path. SPE Reserv Eval Eng 2000;3(4):342–7.
[9] Huenges E, Hurter S, Saadat A, Köhler S, Trautwein U. The in-situ geothermal laboratory Groß Schönebeck—learning to use low permeability aquifers for geothermal power. 27th workshop on geothermal reservoir engineering, 28–30 January 2002.
[10] Roegiers J-C. Elements of rock mechanics. In: Economides MJ, Nolte KG, editors. Reservoir stimulation. Houston: Schlumberger Educational Services; 1999.
[11] Boutéca MJ, Sarda J-P, Vincké O. Constitutive law for permeability evolution of sandstones during depletion. Society of the Petroleum Engineers paper 58717, 2000.
[12] Zhu W, Wong T-F. The transition from brittle faulting to cataclastic flow: permeability evolution. J Geophys Res 1997; 102:3027–41.
[13] Clenell B. Tortuosity: a guide through the maze. In: Lovell MA, Harvey PK, editors. Developments in petrophysics. Geological Society special publication no. 122; 1997. p. 299–344.
[14] David C, Gueguen Y, Pampoukis G. Effective medium theory and network theory applied to the transport properties of rock. J Geophys Res 1990;95(B5):6993–7005.